# Frequency and phase lock-in behind circular cylinder in the presence of random irregular waves

Iskander Abroug and Nizar Abcha*
*Normandie Université, UNICAEN, UNIROUEN, CNRS, UMR 6143 M2C, 14000 Caen, France*

(Received 22 December 2021; accepted 26 May 2022; published 15 June 2022)

In this paper, we present the influence of irregular random waves on the von Kármán street in the wake of an elastically mounted cylinder. The flow is perpendicular to the long axis of the cylinder which is constrained to oscillate transversally. In our experiments, the generated waves are derived from Pierson-Moskowitz and Joint North Sea Wave Project ($\gamma = 3$ or 7) spectra. It was found that the increase of the nonlinearity of the generated waves is accompanied by a decrease of the shedding frequency to half of the pic frequency of the generated waves. Furthermore, the Hilbert transformation was performed to calculate the continuous phases of irregular waves $\theta_\eta$ and that of the Kármán vortex street $\theta_{V_x}$. The temporal evolution of the phase combination $\theta = 2\theta_{V_x} - \theta_\eta$ has been investigated as well. It was found that the time evolution of $\theta$ has a steplike shape, i.e., when $\theta = 0$, this corresponds to a synchronizationlike effect. This approach enables the temporal variability of the synchronization to be quantified in the presence of random irregular waves.

DOI: 10.1103/PhysRevFluids.7.064801

## I. INTRODUCTION

Cylindrical structures involved in offshore systems for energy production are submitted to various solicitations. Among them, the effects of waves and current dominate and may lead to fatigue and structural failures. The process of waves propagating over the cylinder pile has attracted great interest because these structures have been widely used as foundations of marine constructions.

Over the past years, authors of several experimental [1,2] and numerical [3–5] studies have investigated the impact of regular and irregular nonbreaking and breaking waves propagating in deep, intermediate, and shallow water locations on cylinders placed in a mean flow. Although great efforts have been made to numerically [6] and experimentally [7–9] investigate the flow around cylindrical structures, earlier research on the topic mainly focused on the run-up around cylinders and induced wave forces in the presence of regular waves [9,10], irregular waves [11], solitary waves [12,13], and group focused waves [10]. However, a few studies do focus on the von Kármán vortex street appearing behind the cylinder pile in the presence of random irregular waves propagating on the background of a steady current.

The impact of external forces may lead to a significant modification of the characteristics of the von Kármán vortex street appearing behind the cylinder [14]. Authors of experimental [14–18] and numerical [19] studies have found that it is possible to observe a regularization of the von Kármán street, and the frequency lock-in of vortex shedding $f_{sh}$ occurs when the cylinder oscillates harmonically or the flow rate changes harmonically in time [15,20,21]. It was found that external forces can mainly give rise to two different regimes of vortex shedding in the von Kármán street. The subharmonic frequency lock-in occurs when the shedding frequency $f_{sh}$ is half the frequency

*nizar.abcha@unicaen.fr

 

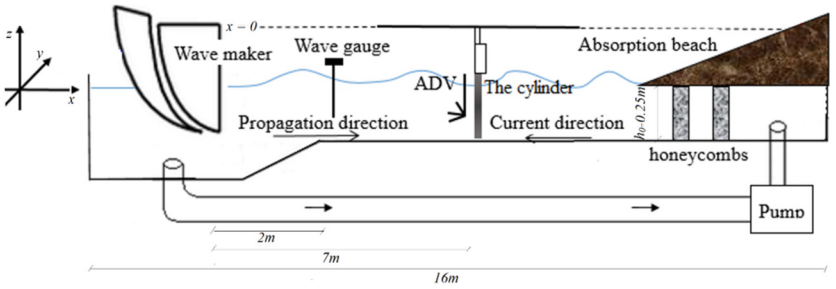


FIG. 1. Experimental setup.

of external oscillations $f_w$, i.e., $2f_{\rm sh} = f_w$, and the harmonic frequency lock-in occurs when the shedding frequency coincides with the frequency of the wave $f_{\rm sh} = f_w$ [17,18].

A link between the flow field and regular waves in the opposite direction was established experimentally by Gunnoo *et al.* [17]. They demonstrated that, with the increase of the amplitude ($a > 0.06\,$cm), the spectral peak in the spectrum of velocity fluctuation appears at $f_{\rm sh} = f_w/2$, corresponding to the subharmonic frequency lock-in phenomenon. In addition, they established regime maps where it is possible to distinguish four regions with different dynamics. Abroug *et al.* [18] investigated the hydrodynamic behavior around a circular cylinder in the presence of group focused waves using the wavelet tool. They found that the dominant frequency components lie in the range $0.45 f_w < f_{\rm sh} < 0.55\, f_w$ in the presence of the subharmonic synchronization regime.

Much less attention has been paid to irregular waves with spectrum type variation in the study of subharmonic frequency lock-in phenomenon. The spatial structure of irregular wave fields depends on the spectrum type, the nonlinearity, and the water depth. It should be noted that the field arising from irregular waves propagating in the vicinity of a vertical cylinder is more complex than that of those arising from harmonic regular waves. Therefore, the influence of a realistic sea state on the characteristics of the wake should be studied extensively.

This paper is an experimental investigation of the effect of random signals on regimes in nonlinear systems with irregular waves. As such, it significantly extends the findings of Refs. [17,18]. Careful experiments at a fine resolution in terms of the independent parameters allow subharmonic regimes, due to irregular waves, to be clearly characterized. This paper is structured as follows. In Sec. II, the experimental setup and the tested irregular waves are introduced. Subharmonic frequency lock-in due to irregular surface waves is presented in Sec. III. Section IV presents results of the phase synchronization between the vortex shedding and irregular waves. Lastly, conclusions of this paper and perspectives are given in Sec. V.

## II. EXPERIMENTAL SETUP AND IRREGULAR WAVE PARAMETERS

The experiments were conducted in the two-dimensional (2D) wave and current flume of Morphodynamique Continentale et Côtière (M2C) Laboratory at Caen University, France. The flume has an Edinburgh Designs LTD piston-type wavemaker at one end and a foam absorber beach at the other end. The last 2 m part of the flume was used as an effective wave absorber. Two special honeycombs are installed below the slope of the absorber beach to decrease disturbances created by the pump and reduce wave reflection. Surface waves were generated at $x = 0$, which was defined as the mean wavemaker position (see Fig. 1). The rigid cylinder model, which is made of Plexiglas with diameter $\mathrm{D} = 0.04\,$m and wet-length $\mathrm{L} = 0.248\,$m under the water level, is placed perpendicularly to the flow direction at $x = 7\,$m from the wavemaker. The cylinder is mounted under an individual elastic base free to oscillate transversely to the flow direction and firmly fixed on the channel structure, whereas the lower part is 2 mm away from the flume bottom. The detailed experimental setup is shown in Fig. 1.

A wave gauge with a sampling rate of 100 Hz, located at $x = 2$ m from the wavemaker, was used as a reference for the input signal. Surface waves propagate on the background of steady current $U = 0.16$ m/s and the corresponding Reynolds number is $\mathrm{Re} = \mathrm{UD}/\nu = 6400$ (where $\nu$ represents the kinematic viscosity of water). The velocity behind the oscillating cylinder was measured using acoustic Doppler velocimetry (ADV). The ADV was placed at a distance D from the streamlined cylinder downflow and measures the three velocity components $V_x$, $V_y$, and $V_z$. The sampling rate for the ADV is 200 Hz in this paper. It is important to mention that all generated waves break after the structure, i.e., at $x > 10$ m, which means that the breaking effect is not considered in this paper.

The experiments presented in this paper were made in the same wave flume and under the same flow conditions as those in Ref. [17]. Additionally, before starting the manipulation of irregular waves, we investigated harmonic waves with frequencies $f_w \in [1.2; 1.9\ \mathrm{Hz}]$ and amplitude $a \in [1.2; 1.9\ \mathrm{Hz}]$. We achieved the same diagram as fig. 3(a) in Ref. [17].

The range of frequencies that comprise generated random waves is 0.4–2 Hz; thus, intermediate water depth conditions are maintained as predicted by linear theory. In fact, the dimensionless water depth is represented by $k_w h_0 \in [0.9; 2.04] > 0.5$, which is considered to align with intermediate water conditions ($k_w$ represents the wave number related to the wave peak frequency $f_w$, and $h_0 = 0.25$ m is the constant water depth). The wave number $k_w$ is calculated using the linear dispersion relation $\omega^2 = g k_w \tanh(k_w h_0)$, where $g$ is the acceleration of gravity, and $\omega = 2\pi f_w$ denotes the wave pulsation. Unidirectional irregular random waves based on the Joint North Sea Wave Project (JONSWAP) [Eq. (1)] [22] and Pierson-Moskowitz [Eq. (2)] [23] spectra were generated:

$$E_{\mathrm{Pierson-Moskowitz}}(f) = \alpha \frac{g^2}{(2\pi)^4} f^{-5} \exp\left[-1,25\left(\frac{f}{f_w}\right)^{-4}\right], \tag{1}$$

$$E_{\mathrm{JONSWAP}}(f) = \alpha \frac{g^2}{(2\pi)^4} f^{-5} \exp\left[-1,25\left(\frac{f}{f_w}\right)^{-4}\right]\gamma^{\delta}, \tag{2}$$

where $\alpha = 0.0081$ corresponds to the Phillips constant, $g$ is the gravity acceleration, and $\sigma$ represents the spectral asymmetric parameter with respect to the spectral peak. The equation describing the JONSWAP spectrum is obtained by multiplying the Pierson-Moskowitz spectrum by the peak enhancement factor:

$$\gamma^{\delta}, \text{ where } \quad \delta = \exp\left[\frac{-\left(\frac{f}{f_w}-1\right)^2}{2\sigma^2}\right], \tag{3}$$

$$\sigma = \begin{cases} 0.07 & \text{for } f \leqslant f_w \\ 0.09 & \text{for } f \geqslant f_w \end{cases},$$

where $\gamma$ is the ratio of the maximum spectral energy to the maximum of the corresponding Pierson-Moskowitz spectrum, and $\sigma$ defines the left- and right-sided widths of the spectrum. Three different peak-enhancement factors were investigated during the experiments, i.e., $\gamma = 1$, 3.3, and 7. The lower value $\gamma = 1$ corresponds to the standard Pierson-Moskowitz formulation, and $\gamma = 7$ provides a narrower spectrum.

The relevant parameters in addition to the relative water depth $k_w h_0$ are the nonlinearity $k_w H_s$ and the Ursell number $U_r = H_s \lambda_w^2 / h_0^3$ ($H_s$ represents the average height of the highest $\frac{1}{3}$ of all waves). During the experimental campaign, 120 cases were tested, which were chosen based on the spectrum type and the nonlinearity $k_w H_s$. It is necessary to wait at least 5 min between two experiments to obtain a near quiescent state, which is confirmed by visual inspection before each test. The wave characteristics of the experimental data used in this paper are listed in Tables I–III.

Fast Fourier transform (FFT) analyses are performed on free surface elevations $\eta$ and transversal velocities $V_x$ to calculate the wave energy and velocity spectra [$S(f)$]. The sampling time is truncated

TABLE I. Summary of the primary Pierson-Moskowitz wave parameters. $f_w$: peak wave frequency; $k_w$: wave number; $H_s$: significant wave height; $U_r$: Ursell number.

| | $f_w$ (Hz) | $k_w h_0$ | $k_w H_s$ | $U_r$ |
|---|---|---|---|---|
| Case 1 | | 0.9 | 0.003 | 0.15 |
| Case 2 | | 0.9 | 0.007 | 0.38 |
| Case 3 | | 0.9 | 0.011 | 0.57 |
| Case 4 | | 0.9 | 0.014 | 0.74 |
| Case 5 | 0.8 | 0.9 | 0.017 | 0.90 |
| Case 6 | | 0.9 | 0.020 | 1.10 |
| Case 7 | | 0.9 | 0.021 | 1.11 |
| Case 8 | | 0.9 | 0.026 | 1.42 |
| Case 9 | | 0.9 | 0.029 | 1.58 |
| Case 10 | | 0.9 | 0.032 | 1.74 |
| Case 11 | | 1.2 | 0.002 | 0.04 |
| Case 12 | | 1.2 | 0.005 | 0.11 |
| Case 13 | | 1.2 | 0.008 | 0.18 |
| Case 14 | | 1.2 | 0.010 | 0.23 |
| Case 15 | 1 | 1.2 | 0.014 | 0.31 |
| Case 16 | | 1.2 | 0.015 | 0.34 |
| Case 17 | | 1.2 | 0.019 | 0.44 |
| Case 18 | | 1.2 | 0.021 | 0.47 |
| Case 19 | | 1.2 | 0.024 | 0.54 |
| Case 20 | | 1.2 | 0.026 | 0.60 |
| Case 21 | | 1.58 | 0.002 | 0.02 |
| Case 22 | | 1.58 | 0.003 | 0.03 |
| Case 23 | | 1.58 | 0.004 | 0.04 |
| Case 24 | | 1.58 | 0.007 | 0.07 |
| Case 25 | 1.2 | 1.58 | 0.008 | 0.08 |
| Case 26 | | 1.58 | 0.011 | 0.11 |
| Case 27 | | 1.58 | 0.012 | 0.12 |
| Case 28 | | 1.58 | 0.017 | 0.17 |
| Case 29 | | 1.58 | 0.018 | 0.18 |
| Case 30 | | 1.58 | 0.019 | 0.19 |
| Case 31 | | 2.04 | 0.001 | 0.01 |
| Case 32 | | 2.04 | 0.002 | 0.01 |
| Case 33 | | 2.04 | 0.001 | 0.01 |
| Case 34 | | 2.04 | 0.003 | 0.02 |
| Case 35 | 1.4 | 2.04 | 0.006 | 0.03 |
| Case 36 | | 2.04 | 0.008 | 0.04 |
| Case 37 | | 2.04 | 0.009 | 0.04 |
| Case 38 | | 2.04 | 0.008 | 0.04 |
| Case 39 | | 2.04 | 0.010 | 0.05 |
| Case 40 | | 2.04 | 0.013 | 0.06 |

to $\Delta T_1 = 60\,\text{s}$, corresponding to 6000 points for wave gauge measurements and to $\Delta T_2 = 187.5\,\text{s}$, corresponding to 37 500 points for ADV measurements:

$$S(f) = 2\,|F(t)|^2, \tag{4}$$

$$F(t) = \int_0^{\Delta T_1} \eta(t) e^{-2\pi i \omega t} dt, \tag{5}$$

$$F(t) = \int_0^{\Delta T_2} V_x(t) e^{-2\pi i \omega t} dt. \tag{6}$$

TABLE II. Summary of the primary JONSWAP ($\gamma = 3.3$) wave parameters. $f_w$: peak wave frequency; $k_w$: wave number; $H_s$: significant height; $U_r$: Ursell number.

| | $f_w$ (Hz) | $k_w h_0$ | $k_w H_s$ | $U_r$ |
|---|---|---|---|---|
| Case 41 | | 0.9 | 0.005 | 0.25 |
| Case 42 | | 0.9 | 0.010 | 0.52 |
| Case 43 | | 0.9 | 0.014 | 0.74 |
| Case 44 | | 0.9 | 0.016 | 0.84 |
| Case 45 | 0.8 | 0.9 | 0.022 | 1.17 |
| Case 46 | | 0.9 | 0.026 | 1.40 |
| Case 47 | | 0.9 | 0.028 | 1.53 |
| Case 48 | | 0.9 | 0.033 | 1.79 |
| Case 49 | | 0.9 | 0.036 | 1.92 |
| Case 50 | | 0.9 | 0.040 | 2.15 |
| Case 51 | | 1.2 | 0.003 | 0.08 |
| Case 52 | | 1.2 | 0.006 | 0.13 |
| Case 53 | | 1.2 | 0.008 | 0.19 |
| Case 54 | | 1.2 | 0.011 | 0.24 |
| Case 55 | 1 | 1.2 | 0.015 | 0.33 |
| Case 56 | | 1.2 | 0.017 | 0.39 |
| Case 57 | | 1.2 | 0.021 | 0.48 |
| Case 58 | | 1.2 | 0.024 | 0.54 |
| Case 59 | | 1.2 | 0.026 | 0.60 |
| Case 60 | | 1.2 | 0.030 | 0.67 |
| Case 61 | | 1.58 | 0.001 | 0.01 |
| Case 62 | | 1.58 | 0.004 | 0.04 |
| Case 63 | | 1.58 | 0.005 | 0.05 |
| Case 64 | | 1.58 | 0.008 | 0.08 |
| Case 65 | 1.2 | 1.58 | 0.011 | 0.12 |
| Case 66 | | 1.58 | 0.013 | 0.13 |
| Case 67 | | 1.58 | 0.016 | 0.16 |
| Case 68 | | 1.58 | 0.019 | 0.19 |
| Case 69 | | 1.58 | 0.023 | 0.23 |
| Case 70 | | 1.58 | 0.026 | 0.26 |
| Case 71 | | 2.04 | 0.001 | 0.01 |
| Case 72 | | 2.04 | 0.003 | 0.02 |
| Case 73 | | 2.04 | 0.004 | 0.02 |
| Case 74 | | 2.04 | 0.006 | 0.03 |
| Case 75 | 1.4 | 2.04 | 0.008 | 0.04 |
| Case 76 | | 2.04 | 0.008 | 0.04 |
| Case 77 | | 2.04 | 0.010 | 0.05 |
| Case 78 | | 2.04 | 0.011 | 0.05 |
| Case 79 | | 2.04 | 0.014 | 0.06 |
| Case 80 | | 2.04 | 0.015 | 0.07 |

All energy forms are normalized by the maximum of the wave and velocity spectra between the cutoff frequencies $[0, 2, 3f_w]$ Hz. The spectrum energy outside this interval is very small, i.e., $< 2\%$, and can be neglected. Figure 2 shows an example of a time series and the corresponding spectrum of three different irregular waves with approximately the same nonlinearity $k_w H_s \sim 0.03$ and derived from Pierson-Moskowitz (Case 10), JONSWAP ($\gamma = 3.3$) (Case 48), and JONSWAP ($\gamma = 7$) (Case 86). As expected, the energy distribution varies from one spectrum to another.

TABLE III. Summary of the primary JONSWAP ($\gamma = 7$) wave parameters. $f_w$: peak wave frequency; $k_w$: wave number; $H_s$: significant height; $U_r$: Ursell number.

| | $f_w$ (Hz) | $k_w h_0$ | $k_w H_s$ | $U_r$ |
|---|---|---|---|---|
| Case 81 | | 0.9 | 0.006 | 0.31 |
| Case 82 | | 0.9 | 0.011 | 0.61 |
| Case 83 | | 0.9 | 0.017 | 0.90 |
| Case 84 | | 0.9 | 0.021 | 1.12 |
| Case 85 | 0.8 | 0.9 | 0.026 | 1.43 |
| Case 86 | | 0.9 | 0.030 | 1.65 |
| Case 87 | | 0.9 | 0.035 | 1.93 |
| Case 88 | | 0.9 | 0.041 | 2.22 |
| Case 89 | | 0.9 | 0.047 | 2.53 |
| Case 90 | | 0.9 | 0.051 | 2.76 |
| Case 91 | | 1.2 | 0.003 | 0.08 |
| Case 92 | | 1.2 | 0.010 | 0.17 |
| Case 93 | | 1.2 | 0.011 | 0.24 |
| Case 94 | | 1.2 | 0.015 | 0.35 |
| Case 95 | 1 | 1.2 | 0.018 | 0.42 |
| Case 96 | | 1.2 | 0.022 | 0.50 |
| Case 97 | | 1.2 | 0.026 | 0.59 |
| Case 98 | | 1.2 | 0.029 | 0.66 |
| Case 99 | | 1.2 | 0.032 | 0.73 |
| Case 100 | | 1.2 | 0.036 | 0.81 |
| Case 101 | | 1.58 | 0.002 | 0.02 |
| Case 102 | | 1.58 | 0.006 | 0.06 |
| Case 103 | | 1.58 | 0.009 | 0.09 |
| Case 104 | | 1.58 | 0.014 | 0.14 |
| Case 105 | 1.2 | 1.58 | 0.017 | 0.17 |
| Case 106 | | 1.58 | 0.023 | 0.24 |
| Case 107 | | 1.58 | 0.028 | 0.28 |
| Case 108 | | 1.58 | 0.029 | 0.30 |
| Case 109 | | 1.58 | 0.032 | 0.32 |
| Case 110 | | 1.58 | 0.037 | 0.37 |
| Case 111 | | 2.04 | 0.003 | 0.01 |
| Case 112 | | 2.04 | 0.003 | 0.01 |
| Case 113 | | 2.04 | 0.004 | 0.02 |
| Case 114 | | 2.04 | 0.008 | 0.04 |
| Case 115 | 1.4 | 2.04 | 0.010 | 0.05 |
| Case 116 | | 2.04 | 0.012 | 0.05 |
| Case 117 | | 2.04 | 0.013 | 0.06 |
| Case 118 | | 2.04 | 0.016 | 0.08 |
| Case 119 | | 2.04 | 0.019 | 0.10 |
| Case 120 | | 2.04 | 0.022 | 0.10 |

## III. SUBHARMONIC FREQUENCY LOCK-IN

To estimate the presence of subharmonic synchronization, the shedding frequency $f_{\mathrm{sh}}$ is found using the FFT of the transverse velocity component $V_x$. Figures 3–5 show spectrograms of the shedding frequency evolution relative to the nonlinearity $k_w H_s$. It is important to mention that the fluctuation spectra are calculated using the averaging procedure. In other words, the time series of $\Delta T_2 = 187.5$ s was recorded and divided into five pieces of 60 s of length (12 000 points) with 50% overlap (6000 points), averaging over 5 FFT amplitude spectra. Without this averaging procedure, the spectra would be very irregular and difficult to analyze properly.

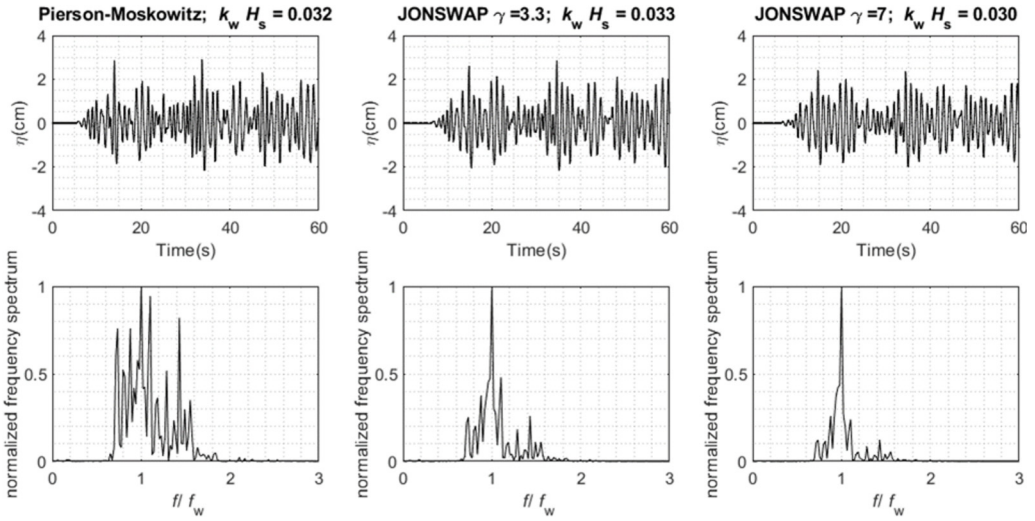


FIG. 2. Three sets of time series and their corresponding spectrum of three irregular waves with approximately the same nonlinearity $k_w H_s$. Frequency spectra are normalized by the maximum of the wave spectrum.

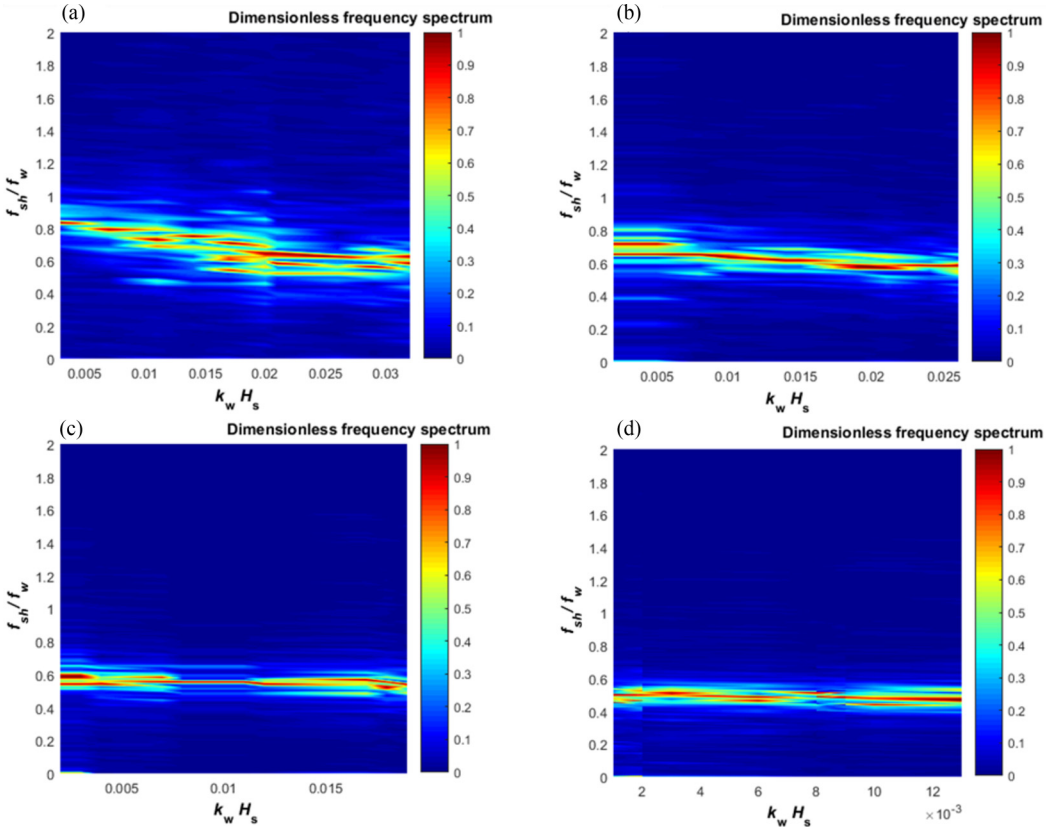


FIG. 3. Spectrograms of Pierson-Moskowitz irregular waves showing the evolution of frequency shedding with relative to wave nonlinearity $k_w H_s$: (a) $k_w h_0 = 0.8$ Hz, (b) $k_w h_0 = 1$ Hz, (c) $k_w h_0 = 1.2$ Hz, and (d) $k_w h_0 = 2.04$ Hz. The color bar represents the dimensionless frequency spectrum.

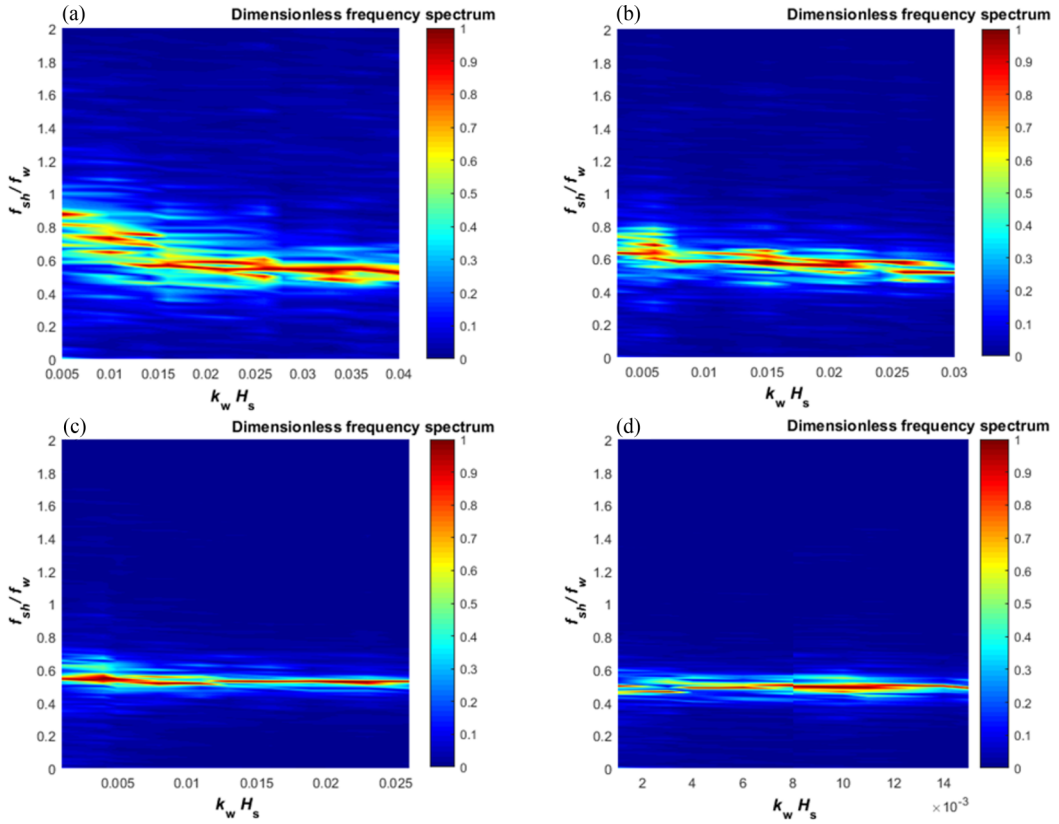


FIG. 4. Spectrograms of JONSWAP ($\gamma = 3.3$) irregular waves showing the evolution of frequency shedding with relative to wave nonlinearity $k_w H_s$: (a) $k_w h_0 = 0.8$ Hz, (b) $k_w h_0 = 1$ Hz, (c) $k_w h_0 = 1.2$ Hz, and (d) $k_w h_0 = 2.04$ Hz. The color bar represents the dimensionless frequency spectrum.

The first finding from the 12 plotted spectrograms is that important changes occur in the spectrum of $V_x$ by increasing the nonlinearity $k_w H_s$. When the nonlinearity increases, two effects can be distinguished: (1) the shading frequency $f_{\mathrm{sh}}$ shifts to lower frequencies; and (2) the amplitude of the velocity fluctuations increases, the spectrum becomes narrower, and the energy becomes mainly concentrated near $f_{\mathrm{sh}} = f_w/2$.

The first effect is in accordance with Gunnoo *et al.* [17], who made the same conclusions in the case of regular waves. The second effect can be related to the regularization of the von Kármán street under the action of the nonharmonic signal. This result appears to confirm conclusions found in Refs. [24–27]. For example, Neiman *et al.* [24] demonstrated that noisy systems can be synchronized by a stochastic driving signal. Under the action of a nonregular signal, nontrivial effects like subharmonic stochastic resonance can appear. Neiman *et al.* [24] added that resonance may appear under certain intensities of external noise.

Moreover, Figs. 3–5 show that the spectrum type has no influence on the evolution of the $f_{\mathrm{sh}} - k_w H_s$ relation. In fact, by switching the spectrum type (i.e., spectral width), the $f_{\mathrm{sh}} - k_w H_s$ relation evolves similarly. Lastly, the water depth $k_w h_0$ has a strong influence on the evolution of the $f_{\mathrm{sh}} - k_w H_s$ relation. In fact, by increasing the water depth, the spectrum energy of $V_x$ is mainly concentrated near $f_{\mathrm{sh}} = f_w/2$, even in the case of low nonlinearities, and this is true for all wave spectra. Consequently, it can be concluded that the water depth plays an important role in the regularization of the von Kármán street and the appearance of subharmonic frequency lock-in phenomena. For shallow water locations, the subharmonic resonance appears in the case of high

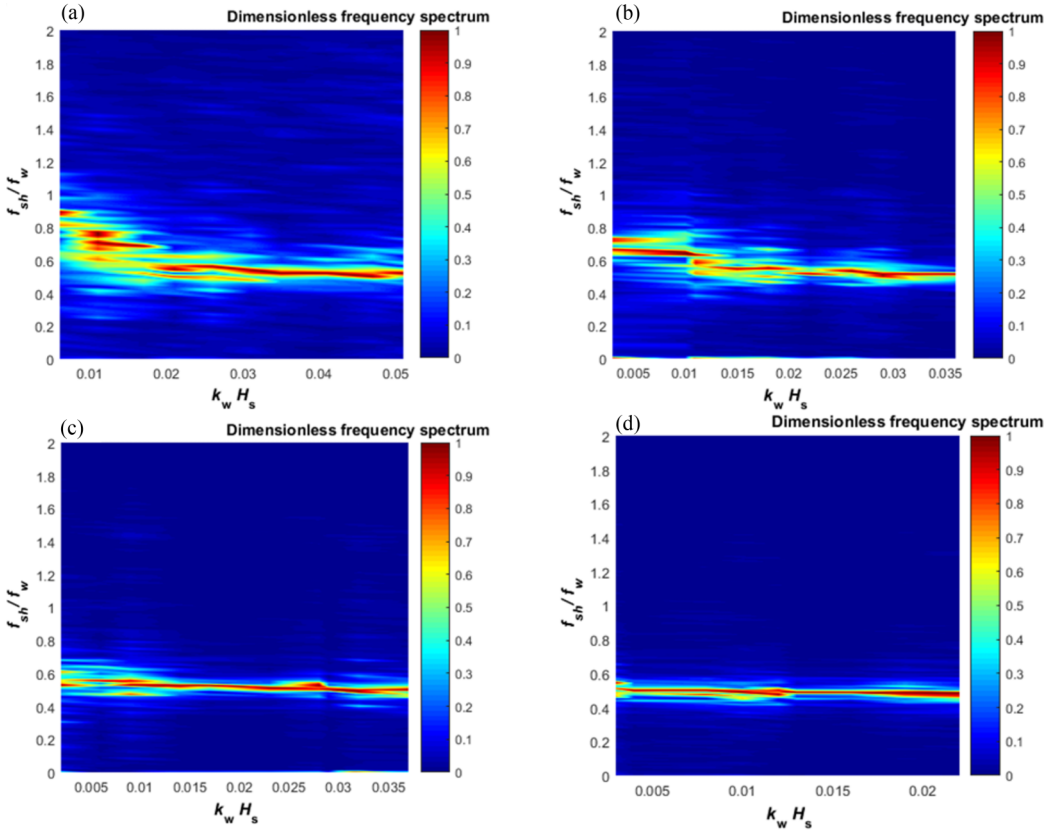


FIG. 5. Spectrograms of JONSWAP ($\gamma = 7$) irregular waves showing the evolution of frequency shedding with relative to wave nonlinearity $k_w H_s$: (a) $k_w h_0 = 0.8$ Hz, (b) $k_w h_0 = 1$ Hz, (c) $k_w h_0 = 1.2$ Hz, and (d) $k_w h_0 = 2.04$ Hz. The color bar represents the dimensionless frequency spectrum.

nonlinearities, whereas for deep water locations, the frequency lock-in phenomenon can appear even for low nonlinearities.

Figure 6 summarizes the evolution of the $f_{\mathrm{sh}} - k_w H_s$ relation. The red background color corresponds to the decreasing trend of the shedding frequency, whereas the green background color corresponds to the relatively stable behavior of the shedding frequency at $\frac{1}{2} f_w$. It is found that, at low nonlinearities, the ratio $f_{\mathrm{sh}}/f_w$ is ∼0.8 in the case of waves with $f_w = 0.8$ Hz (i.e., $k_w h_0 = 0.9$), and by increasing wave nonlinearities $k_w H_s$, we approach a subharmonic synchronization regime.

## IV. SUBHARMONIC PHASE LOCK-IN

The oscillation phase in the wake behind the cylinder is investigated as well to further analyze the subharmonic lock-in phenomenon in the case of irregular random waves. With this aim in view, the instantaneous phase $\theta$ of the system should be introduced [26–29]. Gabor [28] has introduced the definition of $\theta$ based on the concept of the analytical signal. In this frame of mind, the free surface elevation $\eta$ and the velocity $V_x$ can be written, respectively, as $a_{V_x}(t)$ and $b_\eta(t)$ using the analytical representation:

$$V_x(t) = \mathrm{Re}\{a_{V_x}(\mathrm{t})\exp(i\theta_{V_x})\}, \quad |a_{V_x}| = \sqrt{V_x^2 + \hat{V}_x^2}, \quad \theta_{V_x} = \arctan\frac{\hat{V}_x}{V_x}, \tag{7}$$

$$\eta(t) = \mathrm{Re}\{b_\eta(t)\exp(i\theta_\eta)\}, \quad |b_\eta| = \sqrt{\eta^2 + \hat{\eta}^2}, \quad \theta_\eta = \arctan\frac{\hat{\eta}}{\eta}. \tag{8}$$

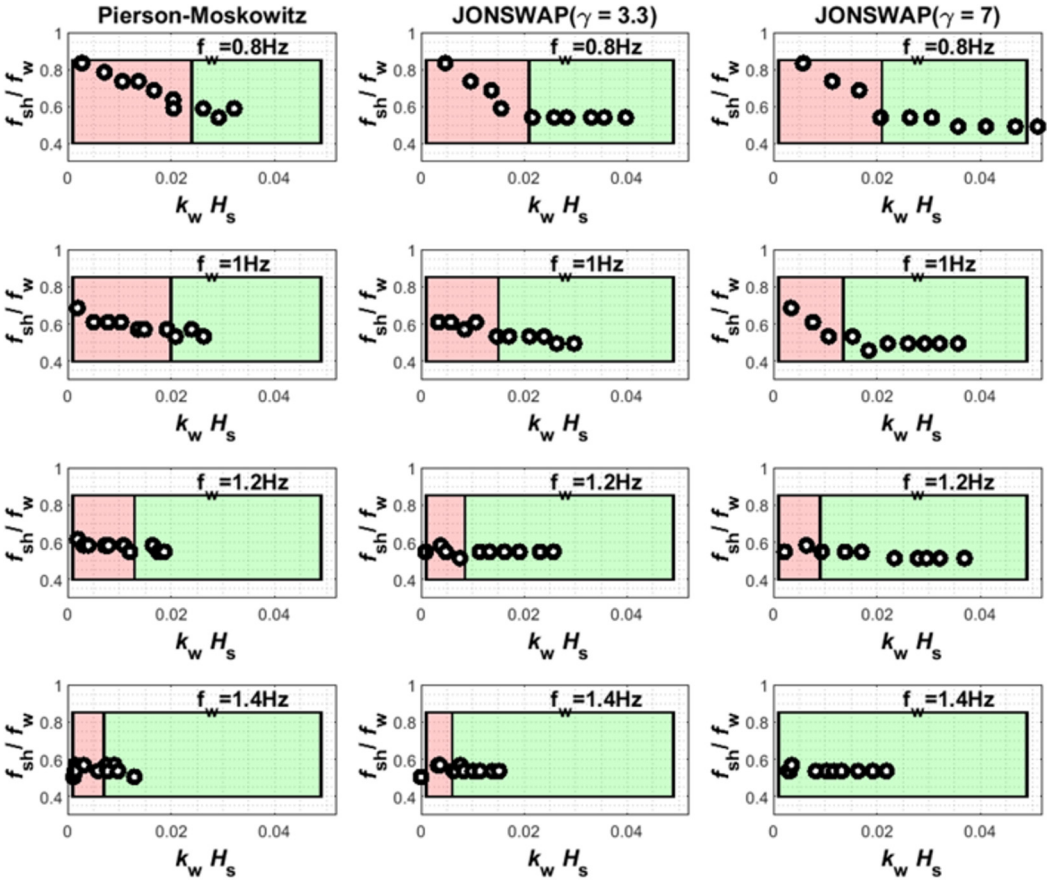


FIG. 6. The evolution of the normalized shedding frequency.

Here, $\hat{V}_x$ and $\hat{\eta}$ are the Hilbert transform of the velocity $V_x$ and the free surface elevation $\eta$, and

$$\hat{V}_x(t) = \frac{1}{\pi}\mathrm{PV}\int_{-\infty}^{+\infty}\frac{V_x(\tau)}{t-\tau}d\tau, \tag{9}$$

$$\hat{\eta}(t) = \frac{1}{\pi}\mathrm{PV}\int_{-\infty}^{+\infty}\frac{\eta(\tau)}{t-\tau}d\tau. \tag{10}$$

Here, PV is taken in the sense of a Cauchy principal value [26]. It is important to mention that the application of the Hilbert transform is especially useful when the signals contain a periodic or quasiperiodic signal. Considering the nonstationary behavior of the generated waves, a relatively narrow bandpass FFT filter was applied to the averaged frequency spectrum of the ADV signal and to the frequency spectrum of the free surface elevation signal to reduce noise and remove components with normalized spectral density $<0.2$. From this procedure resulted an oscillatory signal that can be used for the phase extraction by using the Hilbert transformation. Figure 7 shows the result of applying a bandpass FFT filter on two free surface elevation signals.

Using the ADV phase $\theta_{V_x}$ and the free surface elevation phase $\theta_\eta$, we introduce the phase difference $\theta$ which is expressed as follows:

$$\theta = 2\theta_{V_x} - \theta_\eta. \tag{11}$$

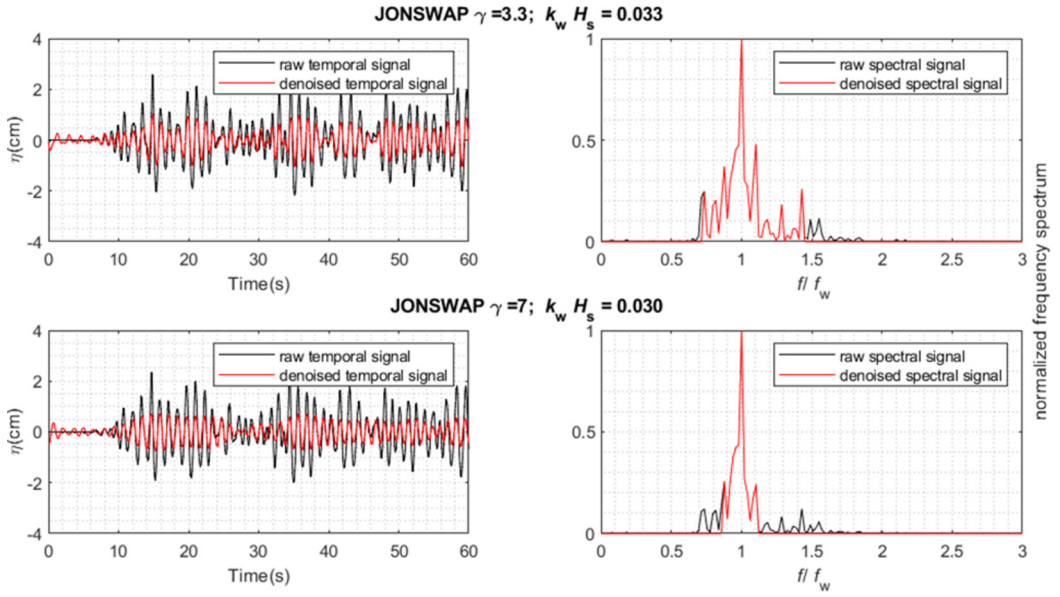


FIG. 7. Comparison between raw signals with signals used for the Hilbert transform after applying a bandpass fast Fourier transform (FFT) filter.

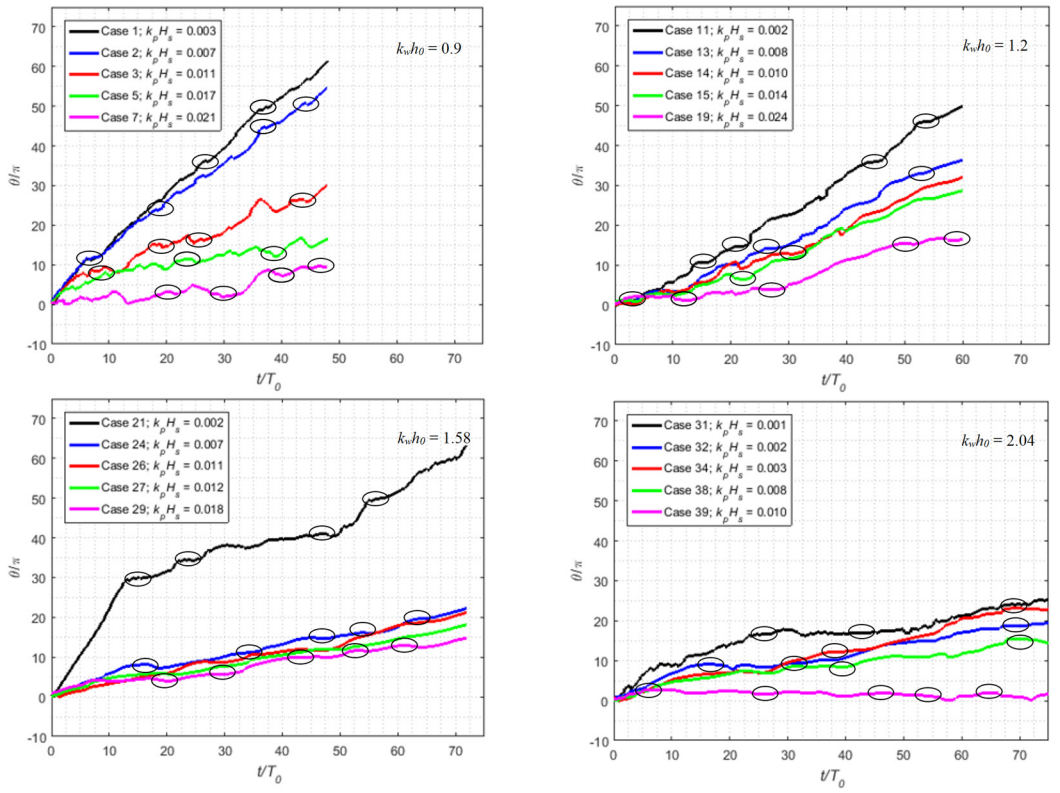


FIG. 8. The temporal evolution of the instantaneous phase difference for Pierson-Moskowitz random waves.

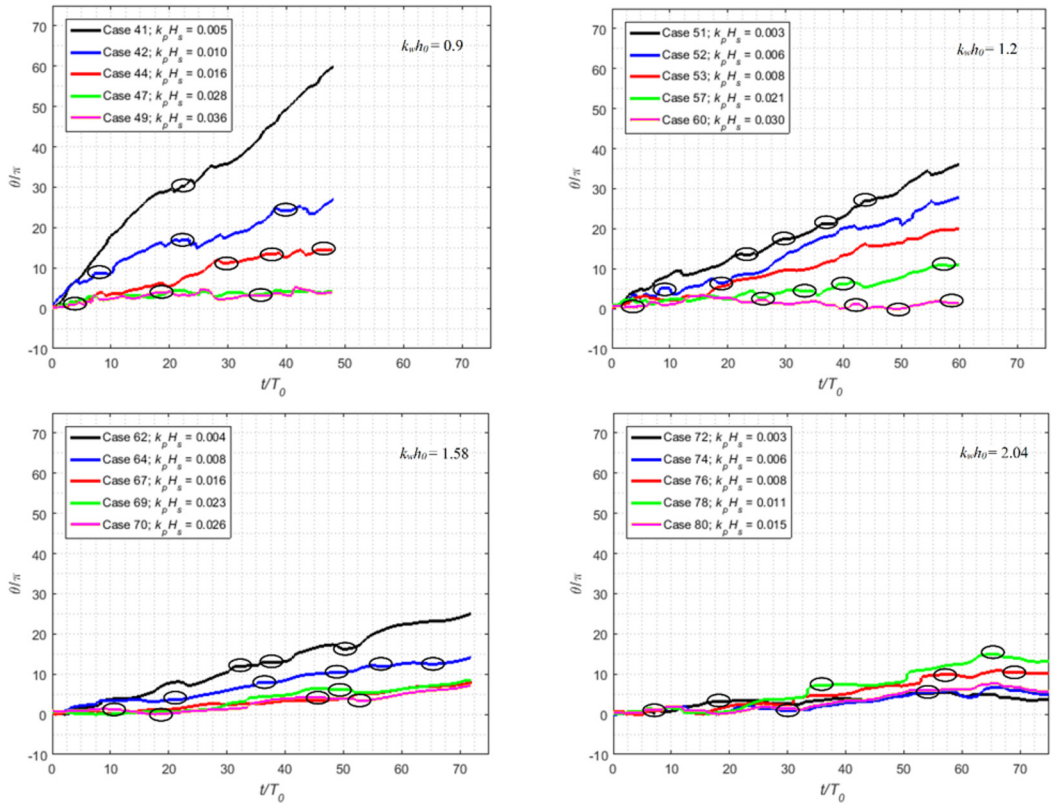


FIG. 9. The temporal evolution of the instantaneous phase difference for JONSWAP ($\gamma = 3.3$) random waves.

If the phase difference $\theta$ is constant (i.e., $d\theta/dt \sim 0$), subharmonic synchronization between the irregular wave and the shedding frequency occurs. Full subharmonic synchronization over the entire sampling time can be observed in a system where sinusoidal waves are generated.

Examples of time series of the phase difference $\theta$ are shown in Figs. 8–10 for different depths and for different types of spectra. Empty ellipses are added to indicate the presence of synchronous epochs. The first main characteristic is a growing rate of the phase difference $\theta$ which monotonically increases with time. During the course of the observation time, the phase is locked for some values of $t/T_0$. There are patterns of nearly constant $\theta$ referring to the phase-locked regimes interrupted by phase rises, indicating a partially synchronized system. In other words, the $d\theta/dt \sim 0$ slope corresponds to a synchronizationlike effect interspersed with fast changes in the phase temporal evolution. Although there are relatively short locking segments, the phase difference displays random walklike behavior without a preferred slope.

The second main characteristic is the strong dependence of the subharmonic synchronization on the magnitude of the external forcing $k_wH_s$ and the water depths $k_wh_0$. If the nonlinearity is relatively low, the phase evolution is close to a linear one, i.e., the phase grows almost uniformly (see Figs. 8–10, $k_wh_0 = 0.9$, $k_wH_s < 0.011$). With increasing wave steepness, the evolution of the phase difference looks like intermittency of relatively large epochs of practically constant phase. In deep water conditions, the length of these plateaus becomes longer, and the duration of the phase-locked segments almost covers the entire sampling time (see Figs. 8–10, $k_wh_0 = 2.04$ and $k_wH_s > 0.01$). These conclusions confirm the results found in Sec. III.

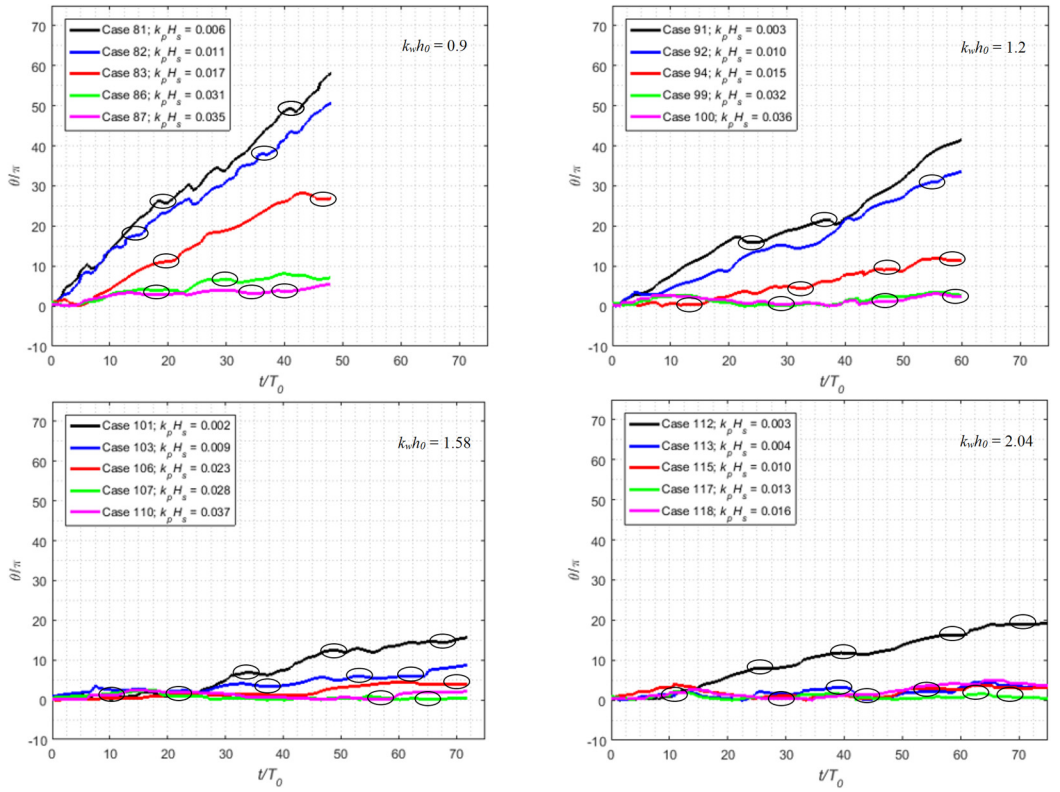


FIG. 10. The temporal evolution of the instantaneous phase difference for JONSWAP ($\gamma = 7$) random waves.

## V. CONCLUSIONS AND PERSPECTIVES

In this paper, we report laboratory investigations on the subharmonic frequency lock-in phenomenon caused by irregular random waves in the wake behind a cylinder. The experiments were carried out using a vertical cylinder with a diameter D = 0.04 m and irregular waves derived from Pierson-Moskowitz and JONSWAP ($\gamma = 3$ or 7) spectra. The water depth was selected to have irregular waves propagating in intermediate water conditions. We used a combination of velocity and free surface elevation phase to find out the synchronization phenomenon in the presence of random waves propagating on the background of a steady current.

It was found that the increase of nonlinearity $k_wH_s$ was accompanied by a narrowing of the velocity spectrum and a decreasing of the shedding frequency $f_{\mathrm{sh}}$. This result is in accordance with conclusions made in Ref. [17], where they only studied regular waves.

To further investigate the oscillatory behavior in the wake, the temporal evolution of the phase difference $\theta = 2\theta_{V_x} - \theta_\eta$ has been investigated. Technically, a narrow bandpass filtering was needed to extract the velocity $\theta_{V_x}$ and free surface elevation phases $\theta_\eta$. Subharmonic synchronization can be defined as the locking between the instantaneous phase of the velocity $2\theta_{V_x}$ and the phase of the external wave force $\theta_\eta$. It was found that $\theta$ approaches zero in the case of high nonlinearities, which corresponds to a synchronizationlike effect. The time evolution of $\theta$ has a steplike shape with intervals where the slope of $\theta = 0$, and this corresponds to the effect of synchronization interspersed with rapid changes. Consequently, the system is partially synchronized.

Moreover, it was found that the subharmonic lock-in is more noticeable in deep water locations. For shallow water conditions, i.e., $k_wh_0 \leqslant 0.9$, the subharmonic synchronization could just occur in

the case of high nonlinearities $k_w H_s > 0.025$. It is important to underline that switching the spectrum type (spectrum width) has no noticeable impact on the subharmonic synchronization phenomenon. In similar contexts, Abroug *et al.* [18] have used the spectral wavelet analysis to investigate the phase synchronization in the presence of group focused waves. It was found that the wave peak frequency does not synchronize in shallow water conditions, i.e., $k_w h_0 < 2.04$. Additionally, they demonstrated that the complex Morlet power spectrum was found to highlight distinctive signatures with changing spectrum width.

The findings of this paper improve our understanding of the oscillatory behavior around cylindrical structure when faced with a steady current and random irregular waves of different nonlinearities and different spectra. It will be interesting to test the combination phase technique to determine if the lock-in occurs in the presence of random irregular waves in field measurements. This detailed examination is useful for practical applications such as assisting engineers in monitoring the impacts on offshore structures and may provide a complementary approach to existing experimental studies.

## ACKNOWLEDGMENTS

The work in this paper was funded by the Normandy Region. I.A. would like to acknowledge the Normandy Region for the PostDoc grantout as part of the DIAgnostique et Disponibilité des installations de production d'Energie électrique à partir des énergies MARines renouvelables (DIADEMAR) project.

[1] H. Gunno, N. Abcha, D. Mouazé, and A. Ezersky, Laboratory simulation of resonance amplification of the hydrodynamic fields in the vicinity of wind farm masts, in *Renewable Energies Offshore*, edited by G. Soares (Taylor & Francis, London, 2015).

[2] Y. Zhiying, B. Huang, A. Kang, B. Zhu. J. Han, R. Yin, and X. Li, Experimental study on the solitary wave-current interaction and the combined forces on a vertical cylinder, Ocean Eng. **236**, 109569 (2021).

[3] Z. Liu, W. Zhao, and D. Wan, CFD study of wave interaction with single and two tandem circular cylinders, Ocean Eng. **239**, 109855 (2021).

[4] D. Qiao, E. Mackay, J. Yan, C. Feng, B. Li, A. Feichtner, D. Ning, and L. Johanning, Numerical simulation with a macroscopic CFD method and experimental analysis of wave interaction with fixed porous cylinder structures, Mar. Struct. **80**, 103096 (2021).

[5] Z. Zhang, J. Tu, Y. He, Z. Han, H. Yang, D. Zhou, and S. Fu, The influence of regular wave and irregular wave on the mechanical characteristics of a triple-cylinder bundle structure, Ocean Eng. **220**, 108379 (2021).

[6] M. Zhao, L. Cheng, and B. Teng, Numerical simulation of solitary wave scattering by a circular cylinder array, Ocean Eng. **34**, 489 (2007).

[7] W. Mo, A. Jensen, and P. L. F. Liu, Plunging solitary wave and its interaction with a slender cylinder on a sloping beach, Ocean Eng. **74**, 48 (2013).

[8] L. Li, J. Zhang, J. M. Chen, and X. Zhao, Experimental study of solitary wave interaction with vertical structures, in *The 28th International Ocean and Polar Engineering Conference* (International Society of Offshore and Polar Engineers, ISOPE, 2018).

[9] M. H. Vested, S. Carstensen, and E. D. Christensen, Experimental study of wave kinematics and wave load distribution on a vertical circular cylinder, Coast. Eng. **157**, 103660 (2020).

[10] S. Shaswat, V. Sriram, A. Shagun, and T. Schlurmann, Experimental investigation of hydrodynamic loading induced by regular, steep non-breaking and breaking focused waves on a fixed and moving cylinder, Eur. J. Mech. B Fluids **93**, 42 (2022).

[11] A. Aggarwal, M. A. Chella, A. Kamath, H. Bihs, and Ø. A. Arntsen, Irregular wave forces on a large vertical circular cylinder, Energy Procedia **94**, 504 (2016).

[12] F. Aristodemo, G. Tripepi, D. D. Meringolo, and P. Veltri, Solitary wave-induced forces on horizontal circular cylinders: laboratory experiments and SPH simulations, Coast. Eng. **129**, 17 (2017).

[13] Y. Ma, B. Tai, G. Dong, and M. Perlin, Experimental study of plunging solitary waves impacting a vertical slender cylinder, Ocean Eng. **202**, 107191 (2020).
[14] O. M. Griffin and S. E. Ramberg, Vortex shedding from a cylinder vibrating in line with an incident uniform flow, J. Fluid Mech. **75**, 257 (1976).
[15] C. H. K. Williamson and A. Roshko, Vortex formation in the wake of an oscillating cylinder, J. Fluids Struct. **2**, 355 (1988).
[16] D. Chen and G. H. Jirka, Experimental study of plane turbulent wakes in a shallow water layer, Fluid Dyn. Res. **16**, 11 (1995).
[17] H. Gunnoo, N. Abcha, and A. Ezersky, Frequency lock-in and phase synchronisation of vortex shedding behind circular cylinder due to surface waves, Phys. Lett. A **380**, 863 (2016).
[18] I. Abroug, N. Abcha, M. Fahd, E. Turki, and E. Ojeda, The hydrodynamic behavior of vortex shedding behind circular cylinder in the presence of group focused waves, Fluids **7**, 4 (2022).
[19] J. S. Leontini, D. L. Jacono, and M. C. Thompson, A numerical study of an inline oscillating cylinder in a free stream, J. Fluid Mech. **688**, 551 (2011).
[20] J. Carberry, J. Sheridan, and D. Rockwell, Forces and wake modes of an oscillating cylinder, J. Fluids Struct. **15**, 523 (2001).
[21] H. M. Blacburn and R. D. Henderson, A study of two-dimensional flow past an oscillating cylinder, J. Fluid Mech. **385**, 255 (1999).
[22] J. Jr., Pierson Willard, and L. Moskowitz, Proposed spectral form for fully developed wind seas based on the similarity theory of S.A. Kitaigorodskii, J. Geophys. Res. **69**, 5181 (1964).
[23] K. Hasselmann, T. Barnett, E. Bouws, H. Carlson, D. Cartwright, K. Enke, J. A. Ewing, H. Gienapp, D. Hasselmann, P. Krusemann, A. Meerburg, A. Muller, D. J. Olbers, K. Richter, W. Sell, and H. Walden, Measurements of wind-wave growth and swell decay during the Joint North Sea Wave Project (JONSWAP), Ergänzungsheft Dtsch. Hydrogr. Z., Reihe A (8°), **12** (1973).
[24] A. Neiman, L. Schimansky-Geier, F. Moss, B. Shulgin, and J. Collins, Synchronisation of noisy systems by stochastic signals, Phys. Rev. E **60**, 284 (1999).
[25] A. Neiman, Synchronisation like phenomena in coupled stochastic bistable systems, Phys. Rev. E **49**, 3484 (1994).
[26] A. Neiman, A. Silchenko, V. Anishchenko, and L. Schimansky-Geier, Stochastic resonance: Noise-enhanced phase coherence, Phys. Rev. E **58**, 7118 (1998).
[27] D. R. Chialvo, O. Calvo, D. L. Gonzalez, O. Piro, and G. V. Savino, Subharmonic stochastic synchronisation and resonance in neuronal systems, Phys. Rev. E **65**, 050902(R) (2002).
[28] D. Gabor, Theory of communication, J. Inst. Elect. Eng. **93**, 429 (1946).
[29] G. V. Osipov, J. Kurths, and C. Zhou, *Synchronization in Oscillatory Networks* (Springer, Berlin, 2007), p. 3.